02

Daewoo Construction Technology Report



플랜트/환경

- 송수펌프 에너지 최적 솔루션을 이용한 에너지 절감 효과 분석
- Application of nanofiltration pretreatment to remove divalent ions for economical seawater reverse osmosis desalination
- 발전배출가스 직접반응을 통한 CO_2포집 및 대량활용 저장기술 개발
- Simplified method for estimating the effect of a hydrogen explosion on a nearby pipeline



송수펌프 에너지 최적 솔루션을 이용한 에너지 절감효과 분석

Energy Reduction Efficiency Analysis Using Optimized Energy Management Solution of Water Supply Pumps

엄정열
플랜트환경연구팀 선임연구원
jungyeol.eom@daewooenc.com

오희경
플랜트환경연구팀 책임연구원
heekyong.oh@daewooenc.com

본 논문은 2015년 세계물포럼, 2015년 대한상하수도학회 공동춘계학술발표회에 발표되었던 논문을 보완하여 게재한 것입니다.

Abstract

Issue of carbon emission and energy consumption is one of the major problems which all countries concern. Government has pushed the energy saving policies such as incentives and penalties and thus domestic waterworks has to consider its own optimized management strategy for saving power consumption. Pump stations for pumping raw water, process water and final water are main energy consumers (more than 90% of total energy consumption) at individual waterworks. Energy loss and waste increases as pumps have been operated at low efficiency for long time. This research introduces thermodynamic method to monitor the real-time pump efficiency using sensors for temperature and pressure at Yeongdeungpo water supply pumping station. In addition, hydraulic performance in conjunction with neural network algorism evaluates the each pump efficiency. Finally this real-time data are used for recommending pump combination and scheduling at the control room. This technology is expected to save energy of 2-3 % compared to the existing operation method and to enable water utilities to optimize pump operation in real time.

Keywords : energy consumption, thermodynamic method, water supply pumping station, neural network algorism, pump combination and scheduling

1_서론

상수도에서 소모되는 에너지양의 약 94%는 물을 이송하기 위하여 펌프를 운영하는 과정에서 소모된다. 따라서 물을 취수, 송수, 배수하는 과정에 있는 펌프장의 펌프를 효율적으로 운영함으로써 에너지 절감에 의한 생산원가 절감뿐만 아니라 최근 국제사회적으로 이슈가 되고 있는 이산화탄소 발생 저감에도 기여할 수 있다. 상수도 송수 시스템의 구성요소로는 펌프와 배수지가 있으며, 상호 연계 운영하고 있다. 운영의 기본은 펌프의 가동율이나 가동 대수의 조절과 배수지의 운전 수위 조정으로 수용가의 수요변동에 대처하고 있다. 실제적으로 송수 펌프들의 관압 유지를 위한 배수지 수위 제어는 정수장이 아닌 수도사업소 역할이기 때문에 정수장에서 송수펌프들의 상태를 실시간으로 모니터링하여 최적의 송수펌프들의 조합으로 소모되는 에너지 절감을 달성해야 한다.

본 연구에서는 과거 수력학적 펌프 진단뿐만 아니라 열역학적인 펌프 진단을 조합함으로써 펌프의 성능을 실시간 모니터링하고, 현재 송수 관압에 적합한 펌프 조합을 운영자에게 제시할 수 있는 에너지 관리 시스템을 적용하여 소모 전력을 절감하고자 하였다.

2_연구 방법

열역학적으로 펌프 운영 현황 모니터링이 가능하도록 압력계, 수온계를 각 펌프에 설치하였으며, 소모전력 평가를 위해 전력량계를 각각 설치하였다. 또한 송수펌프동에 HMI를 설치하여 정수장 중앙제어실에서 실시간으로 송

수펌프 진단 현황을 분석하고 모니터링할 수 있도록 시스템을 구성하였다. 또한 현재 최적 펌프 조합과 유량 증감시 펌프 조합을 제시하여 운영자의 판단을 지원하도록 하였다.

3_결과 및 고찰

3.1. 펌프 조합별 전력원단위, 양정 분포 분석

기존 정수장의 송수펌프 운영방식에 따른 펌프 조합별 전력원단위와 양정 분포를 분석한 결과 전력원단위는 최대 13.5%의 편차가 발생하여 톤당 송수 비용이 약 3원 차이가 발생하는 것을 확인할 수 있었으며, 양정 분포에서도 최적 양정 구간을 벗어나 펌프 운전 효율을 감소시키는 것을 확인할 수 있었다. 따라서 송수유량 및 송수 관압에 따른 최적 조합을 통해 전력원단위 분포를 줄이고, 최적 양정 구간에서 펌프가 가동될 수 있는 펌프 조합을 도출하였다.

3.2 최적 펌프 조합 효과 평가

에너지 관리 솔루션을 이용한 최적 펌프 조합으로 운영

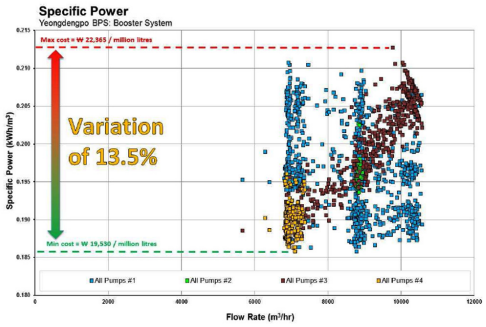


그림 2. 펌프 조합에 따른 전력원단위 편차 분석 결과

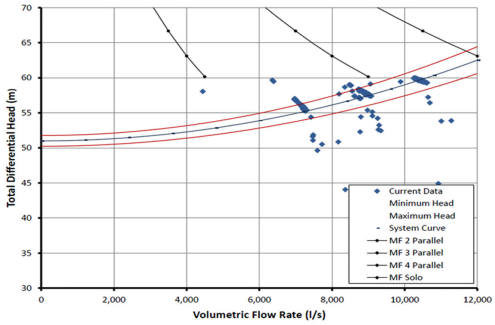


그림 2. 펌프 조합에 따른 전력원단위 편차 분석 결과



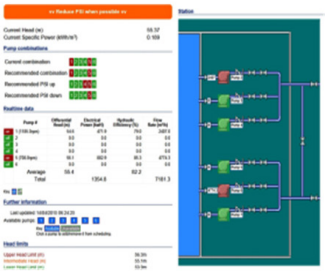
송수 펌프실 현황



펌프별 전력량계 설치



압력계, 수온계 설치(유입, 토출)



제어실 HMI 구축

그림 1. 실증단지 및 시스템 구축 현황

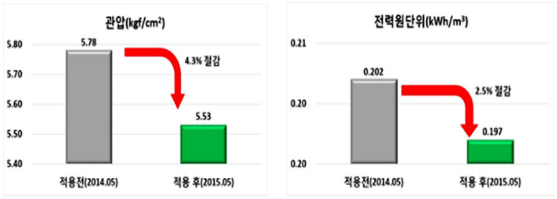


그림 4. 펌프 최적 조합에 의한 송수관압과 전력 절감 효과

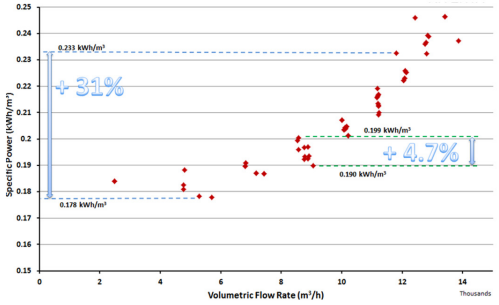


그림 5. 펌프 최적 조합에 의한 전력원단위 편차 분석 결과

한 결과 송수관압과 소모전력 절감효과를 아래 그림에 나타내었다.

에너지 관리 솔루션을 이용한 최적 펌프 조합으로 운영한 결과 전력원단위 편차를 줄일 수 있음을 확인하였다.

4_결 론

에너지 관리 솔루션을 이용하여 송수펌프 조합을 변경한 결과 송수 관압 4.3%, 전력원단위 2.5%의 절감 효과를 얻을 수 있었으며 이를 통해 정수장 소모 전력비를 연간 3천 5백만원 절감할 것으로 예상되었다. 또한 배수지 수위 및 전력피크제 고려시 최대 6%까지 전력비를 절감 할 것으로 기대된다.

참고문헌

1. 박종호, 박한영, 노선민(2010). 실시간 펌프 스케쥴 기법 적용. 유체기계 연구개발 발표회 논문집, pp. 352-355.

사 사

본 연구는 환경부 “차세대 에코이노베이션사업(글로벌탑 환경기술개발사업)”으로 지원받은 과제임(GT-SWS-11-02-007-1)

Application of nanofiltration pretreatment to remove divalent ions for economical seawater reverse osmosis desalination

Minho Park
Plant & Environment Research Team Researcher
minho.park@daewooenc.com

본 논문은 2015년 Desalination and Water Traetment에 11월 20일에 채택되어 출간중인 논문을 재게재한 것입니다.

Abstract

To minimize scale formation potential in applications of reverse osmosis (RO) membranes as a pretreatment unit, relatively loose nanofiltration (NF) membrane systems coupled with ultrafiltration (UF) were used to remove divalent ions from seawater. However, the UF did not reject any ions because of pore size. The rejection of divalent ions by NF was in order of sulfate (>95 %), magnesium (>60 %), and calcium (>30 %) in every rejection experiment based on water recovery rate (40, 50, 60, 70, and 80 %). In the UF/NF/RO hybrid pilot system, most of the divalent (>99 %) and the monovalent (>97 %) ions were effectively rejected with slightly increased divalent ion rejection compared to the UF/RO system. Seawater temperature influenced rejection of ions with regards to either the diffusion- or convection-dominant transport of ions through the membrane pores. Electric power consumption was also compared between the UF/NF/RO process and the UF/RO process. For different salinity conditions (28,000 and 45,000 mg/L of total dissolved solids) the lowest energy consumption by NF/RO was 3.3 and 6 kWh/m3 with recovery of 80 % for NF and 40 % for RO, respectively.

Keywords : Desalination; Nanofiltration; SWRO; Divalent ions; Scaling; Energy consumption

1_INTRODUCTION

Over the last few decades, desalination has been recommended as a possible solution to the water shortage problem worldwide [1]. Among various desalination processes, reverse osmosis (RO) membrane processes have achieved high efficiencies (>99 %) in removing salts to produce fresh water from seawater [1, 2]. According to the 24th International Desalination Association(IDA) Worldwide Desalting Plant Inventory (2012) [3], 747 new plants were established in 2011. The report estimated the global desalination capacity to be 77.4 million m^3/d (20,449 MGD) with 15,988 plants; this market growth was due to development of advanced seawater RO (SWRO) desalination techniques with improved energy efficiency. However, SWRO desalination still has limitations, such as fouling, scaling, high energy cost, and limited water recovery [4, 5]. Among those, scaling has been one of the significant problems in SWRO desalination process. Due to high salt rejection of SWRO, the inorganic compounds are concentrated and precipitate on the membrane surface, which leads to scaling. This can cause flux decline, which increases the energy consumption and maintenance costs especially in RO system [1, 2, 6]. To overcome the scaling problem, many research groups have applied various pretreatments to remove salts prior to RO process; acidity (i.e., pH) adjustment, addition of anti-scalants, and NF membrane treatment [7, 8]. Among various pretreatment options, nanofiltration (NF) is effective in preferentially rejecting divalent ions from seawater [7, 9, 10]. Peter Eriksson et al. (2005) reported that NF membrane rejected sulfate ions with rejection efficiency higher than 99 % and other divalent cations at 80–95 % [9]. Another study has investigated the rejection of compounds

leading to scaling by commercially available NF membranes, where 60 % rejection of bicarbonate, an important ion to produce $CaCO_3$ scalant, was presented, and 60–70 % of rejection of various other divalent ions by NF was reported [11].

Energy consumption is another considerable factor in SWRO desalination. Although SWRO desalination is more economical than thermal desalination, energy consumption in SWRO process needs to be further reduced since it is related to total water production cost. The energy consumed by various SWRO systems investigated are in the range 3.7–5.3 kWh/m^3 [12-14]. According to Drioli et al. (2002, 2006), NF followed by SWRO system showed energy consumption of 4.5 kWh/m^3 [15] and 3.7 kWh/m^3 [16] in two different studies. The estimated energy consumption may vary depending on RO or NF/SWRO desalination system capacities, but it is important to optimize energy consumption for desalination designed for various purposes.

Both salt concentration and temperature of seawater are important parameters influencing the efficacies of NF/SWRO desalination processes. For example, as seawater temperature increases, salt rejection by NF membranes decreases (i.e., from diffusion dominant process), and water permeation increases according to the Arrhenius relation [17]. Different seawater temperatures and the percentage salt rejection have been monitored for NF/SWRO processes to evaluate the effect of seawater temperature on desalination performance using membrane. In this study, to determine optimal operation conditions for NF/SWRO desalination, the salt rejection efficiencies of NF membranes as a pretreatment system for SWRO membranes were investigated under various recovery conditions. The effect of feed water temperature on NF membrane performance was demonstrated, and energy consumptions were monitored with two different membrane desalination systems (either NF/SWRO or SWRO).

2_MATERIALS AND METHODS

2.1. Sampling site and pilot system description

The pilot plant system used for this study was located near the city of Incheon, Korea. The feed seawater, obtained from the Yellow Sea, was purchased from a seawater distributor. The sea water was filtered by the distributor using sand-filtration. Characteristics of the feed water are listed in Table 1. The temperature and the total dissolved solid (TDS) concentration of the seawater used in UF feed water were measured on-site; these values exhibited seasonal fluctuations, from 3.6 °C and 31,000 mg/L in winter to 28.5 °C and 28,000 mg/L in summer.

The pilot plant system consisted of UF/NF/RO modules in series to compare the performances of UF/NF, UF/RO, and UF/NF/RO systems, with respect to water qualities and energy effectiveness. A schematic of the NF/RO hybrid pilot plant is illustrated in Fig. 1 and a detailed description of membrane modules used in each system is summarized in Table 2. The UF membrane modules were equipped with polysulfone hollow-fiber UF membranes (GUF-6050ES, Pure Envitech Co., Ltd., Korea). Six modules of 4-inch polyamide-based thin film composite (TFC) NF membranes (NF270-4040, Dow Filmtec, Midland, MI) in one pressure vessel were used as the NF unit to remove divalent ions prior to SWRO. Permeate of the NF unit was used as feed water for a 4-inch polyamide-based TFC RO membrane (SW30-4040, Dow Filmtec, Midland, MI) unit (6 modules in one vessel).

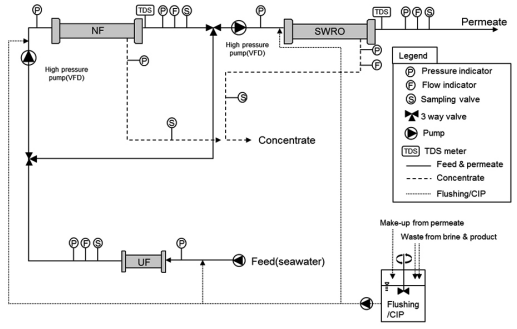


Fig. 1. Schematic flow diagram of NF/RO hybrid pilot plant. Feed water was filtrated through UF process to evaluate the exclusive effect of salts on NF, RO and NF–RO process

A high-pressure displacement pump (APP 1.8, Danfoss™, Denmark) was placed in front the NF and RO units. Flow rate was controlled by a variable frequency device (VFD) (Model iG5A, LSIS Co., Ltd., Korea) to feed a pre-designated flow rate. As

Table 1 Feed water characteristics

Anions	Concentration (mg/L)		Cations	Concentration (mg/L)	
	Seawater	Designed seawater[a]		Seawater	Designed seawater[a]
Chloride	17,000 ± 2,500	27,000 ± 1,600	Sodium	9,700 ± 390	16,000 ± 1,000
Sulfate	2,300 ± 140	2,400 ± 140	Magnesium	1,100 ± 46	2,000 ± 140
Bromide	44 ± 6.2	63 ± 14	Calcium	330 ± 17	620 ± 70
Fluoride	0.90 ± 0.04	6.3 ± 8.4	Potassium	310 ± 17	580 ±36

[a]Reuse of RO concentrate as feed water for simulating Middle East sea (TDS = 45,000 mg/L)

Table 2 Description of selected membranes provided by manufacturer and other previous researches

	UF	NF	RO
Membrane model	GUF-6050ES	NF270-4040	SW30-4040
Manufacturer	Pure Envitech	Dow Filmtec	Dow Filmtec
Membrane type	Polysulfone	Polyamide Thin-Film Composite	Polyamide Thin-Film Composite
MWCO (Da) / Pore size	100K/0.1μ m [a]	300 [21]/0.84 nm [22]	Not available
Pure water permeability ($L\ m^{-2}\ h^{-1}\ bar^{-1}$)	204.1 [b]	14.0 [22]	1.23 [22]
Salt rejection (%)	–	40–60 [c], >97 [d]	99.4 [e]
Zeta potential at pH 7 (mV)	–	– 32.6 [23] approx. –24 [22]	approx. –14 [22]
Root mean square roughness (nm)	–	9.0 (±4.2) [23]	approx. 71 [24]
Contact angle (°)	–	28 (±2) [22]	62.0 (±7.2) [22]

[a] Provided by manufacturer
[b] Provided by manufacturer (0.98 bar pressure)
[c] Tested condition by manufacturer (500 mg/L $CaCl_2$, 5 bar pressure)
[d] Tested condition by manufacturer (2000 mg/L $MgSO_4$, 5 bar pressure, recovery 15 %)
[e] Tested condition by manufacturer (32000 mg/L NaCl, 55 bar pressure, recovery 4~10%)

shown in Fig. 1, electric devices were equipped and calibrated to measure the operational parameters, such as pressure (Model KP-200, Corea Flow Co., Ltd., Korea), flow rate (Type 2536 Rotor-X, Georg Fischer Ltd., Switzerland), temperature (KT-10, Corea Flow Co., Ltd., Korea), and electrical power consumption (LGRW34-2210, LSIS Co., Ltd., Korea); all the data obtained were stored in a data acquisition system. The UF, NF, and RO units were automatically operated using a programmable logic controller (PLC) under the designed experimental conditions. Conventional cleaning-in-place (CIP) was applied to offset the effects of previous.

2.2. Pilot plant operation

The UF/NF, UF/NF/RO, and UF/RO experiments were conducted at varying recovery ratios to evaluate salt rejection and energy consumption, as tabulated in Table 3. Operation time and feed flow rate for each experiment was 150 min and 40 m^3/d, respectively. Two different seawater samples were applied as feedwater to NF and RO membranes. One was seawater from the Yellow Sea, and the other was a designed seawater to simulate Middle East seawaters, so as to investigate the applicability of the NF/RO system under relatively higher salinity. All the feed seawater was filtered using UF membranes and fed to NF and RO membranes. For the production of designed seawater, RO concentrate was prepared with TDS of 45,000 mg/L, at ~40 % recovery, and 6 m^3 of RO concentrate was used for each set of experiment. Feed, permeate, and concentrate were collected thrice from each experiment through sampling valves and were analyzed in

Table 3 Operational conditions for evaluating NF, RO and NF/RO perfomance

Feed water	Process (Membrane)	Qf [a] (m3/d)	TDSf [b] (mg/L)	Recovery (%)		
				NF (flux: lmh)	RO (flux: lmh)	System
Seawater	NF270	40	28,000	40 ~ 80 (13 ~ 26)	–	40~80
	NF270–SW30	40	28,000	80 (26)	12.5 ~ 62.5 (5 ~25)	10~50
	SW30	40	28,000	–	10 ~ 50 (4 ~20)	10~50
Designed Seawater	NF270	40	45,000	40 ~ 80 (13 ~ 26)	–	40~80
	NF270–SW30	40	45,000	80 (26)	12.5 ~ 50 (5 ~ 20)	10~40
	SW30	40	45,000	–	10 ~ 40 (4 ~16)	10~40

[a] Qf indicates flow rate of feed water.
[b] TDSf indicates TDS of feed water.

terms of salt concentration (mg/L) to observe the salt rejection. Specific energy consumption (kWh/m^3) was calculated at 25 °C to estimate economic feasibility through measurements of both energy consumption and permeate volume during operation. For comparison, the energy consumption was measured both before and after the operation, by an electric meter (LGRW34-2210, LSIS Co., Ltd., Korea). Changes in pressure, flow rate, and temperature were monitored to demonstrate the effects of the operating conditions on membranes performance of UF, NF, and RO systems. Feed flow rate and recovery of the UF unit were set at 45 m3/h and 95 % (flux = 59 lmh) to maintain a constant feed flow rate to the NF and RO units. Feed flow rate was determined considering membrane cleaning time and recovery ratio. The initial transmembrane pressure (TMP) was 0.4 bar. Each operation cycle was 30-min long (filtration for 28 min, back washing for 1 min, and flushing for 1 min).

NF experiments were performed with different recovery ratios from 40 % (flux = 13 lmh) to 80 % (flux = 26 lmh) and evaluated in terms of salt rejection (including divalent ions) and energy consumption, to find the optimum condition for NF operation. To compare the NF/RO combination with RO, the end salt rejections and specific energy consumptions were assessed with identical overall recovery ratios varying from 10 % (flux = 4 lmh) to 50 % (flux = 20 lmh). Recovery ratio of NF in the NF/RO operation was set to 80 %, which gives the lowest specific energy consumption compared to other recovery ratios (Fig. 7). As the NF permeate was fed to the RO unit in the NF/RO process, the characteristics of the NF permeate directly influence RO performance. The effect of temperature on NF performance was intermittently monitored for each set of operations. Seasonal experiments were conducted, from winter to summer, with both seawater and the designed seawater. CIP was conducted when TMP of the UF membrane reached 1.5 bar, then, TMP was restored to the initial value of 0.4 bar. The chemicals used for cleaning the UF were 0.1 M citric acid and 0.5 % sodium chlorite, and 0.2% hydrochloric acid, 1.0 % sodium hydrosulfite, and 0.1 % sodium hydroxide were used for cleaning of NF and RO. No changes in the normalized performance data of NF and RO were detected after CIP was applied on the UF system, followed by the NF and RO systems, indicating that NF and RO were not fouled by organic matters or scalants. During operation, there were no significant TMP increase and flux decline in the NF and RO systems; hence, no antiscalant was added in this study and no study on the comparison of scale formation was carried out.

2.3. Water quality characterization

Temperature, conductivity, and TDS were all measured in situ. Other water quality characteristics were also analyzed after prefiltration using 0.7-μm glass macro-fiber filters (GFF, Whatman, Maidsone, England). Ions were analyzed using ion chromatography: ICS-90 (Dionex, Sunnyvale, CA, USA) equipped with IonPac AS14 column (Dionex, USA) for anion analysis and DX-120 (Dionex, USA) equipped with IonPac CS12A column (Dionex, USA) for cation analysis. For anion analysis, 3.5 mM sodium carbonate and 1.0 mM sodium bicarbonate eluent (Dionex AS14 eluent concentrate, Thermo Scientific) were used, and 2.0 N sulfuric acid (Dionex, Sunnyvale, CA, USA) was used for anion regenerant. For cation analysis, methane sulfonic acid was purchased from Sigma-aldrich and used for eluent. Tetrabutylammonium hydroxide solution (Fluka) was used as the cation regenerant solution. Silver-bonded resin cartridges (On-guard Ag, Dionex, Sunnyvale, USA) were used to remove chloride and sulfate anions prior to the IC analysis. Samples were diluted with different dilution factors to obtain reliable ion concentrations in the range 0.5–20 mg/L. Each permeate water quality from the experiments is listed in Table 4.

Table 4. Permeate water quality of UF–NF, UF–RO, and UF–NF–RO.

Recovery (%)	Concentration (mg/L)						
	Chloride	Sulfate	Sodium	Magnesium	Calcium	Potassium	TDS
UF–NF							
40	23600 (±700)	130 (±30)	15100 (±400)	770 (±60)	400 (±2)	550 (±10)	24470 (±70)
50	22000 (±1800)	190 (±20)	14100 (±1100)	630 (±60)	390 (±3)	540 (±9)	24080 (±50)
60	22600 (±1600)	166 (±50)	14500 (±900)	660 (±40)	360 (±6)	530 (±3)	24140 (±60)
70	22700 (±1100)	180 (±40)	15700 (±200)	710 (±40)	380 (±2)	550 (±9)	23220 (±80)
80	23100 (±1900)	120 (±20)	15300 (±300)	730 (±50)	370 (±10)	550 (±30)	22630 (±60)
UF–RO							
10	520 (±20)	27 (±1)	540 (±6)	7 (±0)	2 (±0)	22 (±0)	1177 (±30)
20	440 (±2)	16 (±1)	420 (±5)	4 (±0)	1 (±0)	16 (±0)	931 (±0)
30	350 (±10)	11 (±1)	330 (±10)	3 (±0)	1 (±0)	13 (±0)	704 (±0)
40	350 (±5)	9 (±0)	310 (±4)	3 (±0)	1 (±0)	12 (±0)	647 (±0)
UF–NF–RO							
10	920 (±40)	1 (±0.5)	720 (±10)	2 (±0)	1.4 (±0)	23 (±1)	154 (±0)
20	640 (±10)	0.5 (±0)	520 (±10)	1.3 (±0)	0.9 (±0)	16 (±1)	102 (±0)
30	540 (±50)	0.3 (±0)	440 (±4)	1.1 (±0)	0.8 (±0)	13 (±1)	102 (±0)
40	590 (±50)	0.3 (±0)	400 (±21)	1 (±0)	0.8 (±0)	12 (±1)	102 (±0)

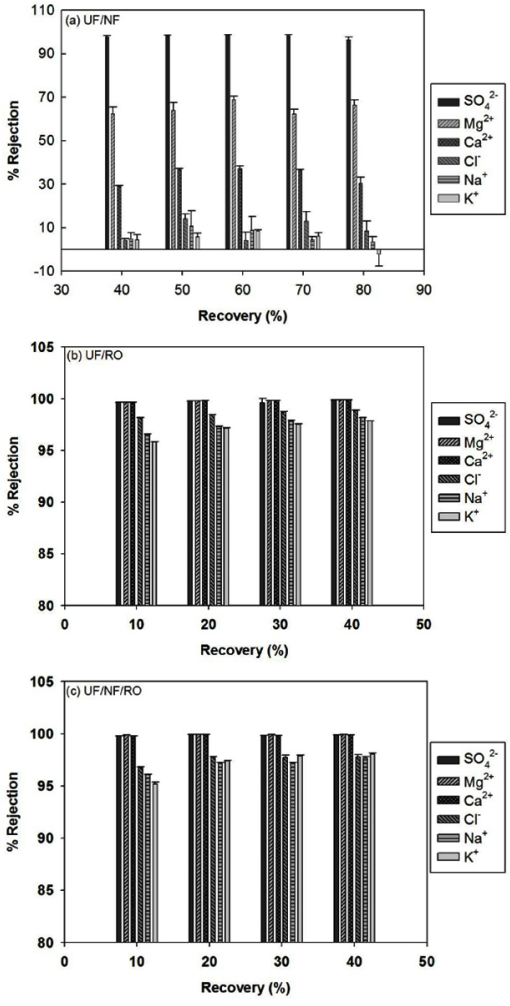


Fig. 2. Monovalent and divalent ion rejection (%) as function of different recoveries, during the (a) UF/NF, (b) UF/RO, and (c) UF/NF/RO operations.

3_RESULTS AND DISCUSSIONS

As shown in Fig. 2, an NF membrane can effectively reject sulfate ($SO4^{2-}$) and two cations (i.e., Mg^{2+}, Ca^{2+}) at high and moderate percentages, respectively, as expected from electrostatic repulsion interactions with the negatively charged membrane surface and the subsequent Donnan exclusion [18]. The NF membrane rejects Mg^{2+} more effectively than Ca^{2+}; however, molar concentrations of the two cations in the NF permeate were similar each other (Ca^{2+} concentration of 12.9 mM and Mg^{2+} concentration of 29.0 mM). Thus, it seems that any difference in rejection percentage between the two cations with NF membrane did not result from the different characteristics of the ions, such as size of the hydrated ions. As expected, the NF membrane did not reject all the monovalent ions, at virtually no rejection, from the UF permeate, as shown in Figs. 2(a) and 3(a). The two combinations of UF/RO and UF/NF/RO did not show any significant ion rejection performance (Figs. 2(b) and (c)).

Effects of recovery of the membrane systems were demonstrated in terms of sulfate rejection, with only the RO and NF/RO membranes. When the RO membrane was solely used (without NF membrane as pretreatment), sulfate levels in the permeates decreased with increasing recovery ratios, indicating that the process was dominated by diffusion over convection transport phenomena. However, the NF/RO combined system was not affected by variations in recovery ratios, probably due to fairly good sulfate rejection effectiveness of the NF membrane, as shown in Figs. 2(a) and 3(b). Rejection of divalent cations was also influenced by system recovery: even at relatively low recovery levels, Mg^{2+} levels decreased (i.e., increase of rejection) with increasing recovery, especially for the RO system, probably due to Donnan exclusion along with subsequent sulfate rejections. Calcium concentration in the permeate was less affected than magnesium, however, the Ca^{2+} levels still noticeably decreased, as shown in Fig. 4(b), for both RO and NF/RO systems.

Convection dominant process, with respect to ion rejection by NF membrane, was demonstrated by filtration experiments at temperatures in the range 5.0–28.5 °C; decreased ion concentrations and TDS rejection were measured at relatively high seawater temperatures with increased permeate flux due to lower viscosity and corresponding lower membrane resistance (Fig. 5). In addition, this phenomenon can be explained by Arrhenius relation [17], This Arrhenius type of relation can elucidate the permeation behavior of either certain solutes or solvents through a membrane with increasing temperature, in terms of activation energy and permeability coefficient. Otherwise, indirectly, this result can also be explained by membrane morphological changes, as discussed by Park et al. [19] and Sharma et al. [20]. According

to Park et al., as temperature of feed water increased from 7 to 25 °C, molecular weight cutoff (MWCO) of the membranes also increased. Sharma et al. investigated the effect of temperature (5–41 °C) on two thin-film composite NF membranes and the results indicated that the morphology and structure of the polymer-based membrane barrier layer changed with increasing temperature. Membrane swelling has been also observed at different temperatures, as reported by Nilsson et al. At a higher temperature of 50 °C, the degree of swelling was more than that at 20 °C due to the increase in polymer flexibility at higher temperatures. Sulfate rejection was not affected by varying temperature and subsequent change in permeate flux, indicating that electrostatic repulsion was dominant over any other transport, for rejection of divalent sulfate anion.

Efficient operation of the NF/RO system was compared with the RO system, in terms of specific energy consumption (kWh/m^3) and TDS rejection, with different system recoveries. As shown in Fig. 6, the specific energy consumption of the NF/RO system decreased with increasing recovery ratio, similar to the RO system, with recovery ratios of 80 % for the NF unit and 10–40 % for the RO unit. The specific energy consumption of the NF/RO system ranged from 3.3 kWh/m^3 at 40 % RO recovery to 9.9 kWh/m^3 at 10 % RO recovery, with NF recovery ratio at 80 %, for the relatively low-salinity seawater (TDS = 28,000 mg/L). In case of high-salinity seawater (TDS = 45,000 mg/L), the specific energy consumption of NF/RO (at NF recovery of 80 %) ranged from 6.1 kWh/m^3 with 40 % RO recovery to 19.8 kWh/m^3 with 10 % RO recovery. The lowest levels of energy consumed by NF/SWRO (i.e. 3.3–6.1 kWh/m^3) are consistent with reported specific energy consumption values (3.7–5.3 kWh/m^3) [11-15]. However, when the recovery ratio decreased to 10–20 %, the specific energy consumption significantly increased to 9.8–19.8 kWh/m^3.

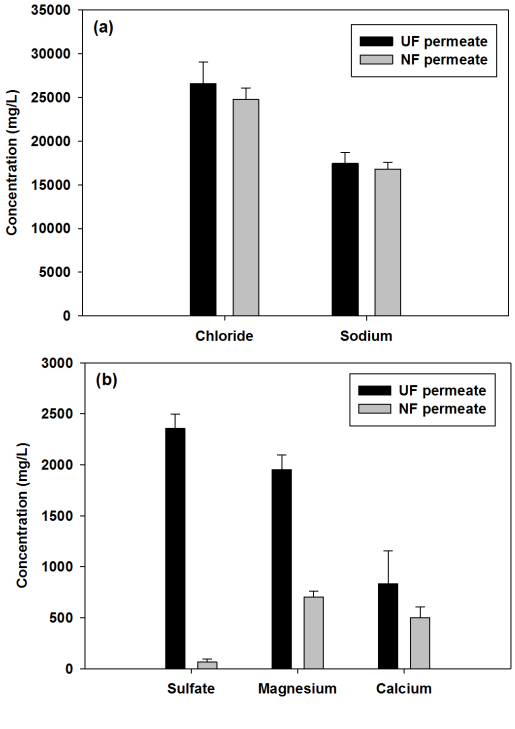


Fig. 3. Concentration of (a) monovalent ions and (b) divalent ions in UF permeate (NF feed water) and UF/NF permeate (SWRO feed water).

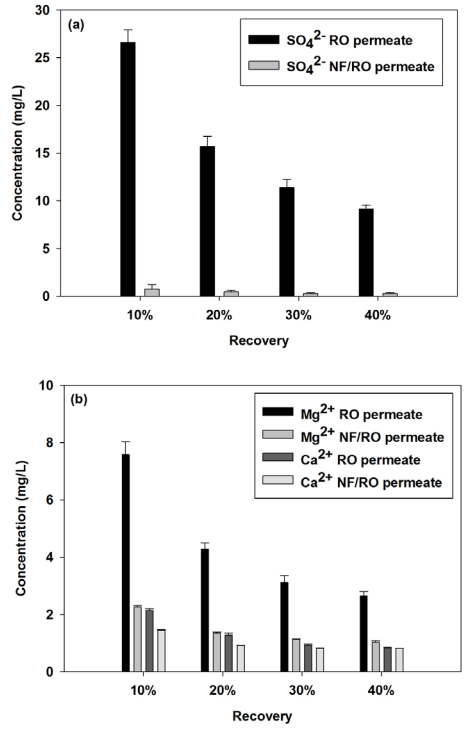


Fig. 3. Concentration of (a) monovalent ions and (b) divalent ions in UF permeate (NF feed water) and UF/NF permeate (SWRO feed water).

Patterns of increasing TDS rejection of the NF/RO system were similar to the ones of the RO system. This demonstration with the NF/RO system was obvious at a relatively low TDS (~28,000 mg/L), generally found in the seas around Korea (Fig. 6(a)). However, when the salt levels of feed seawater increased to simulate a Middle East seawater TDS (~45,000 mg/L), the efficiencies in energy consumption and TDS rejection of the NF/RO system somewhat decreased compared to the RO system, but, the patterns were the same (Fig. 6(b)). The difference in energy consumption and TDS rejection was not significant; thus, it is probably compensated by somewhat increased water qualities, in terms of ion concentration levels in the final feedwater treated by the NF/RO system. Based on the specific energy consumption values for various types of seawaters containing low to high salt concentrations, the probable optimal operating condition for the NF/SWRO hybrid system can be the recovery ratio at 80 % for NF and 40 % for RO, which give the lowest specific energy consumption with relatively high salt rejections.

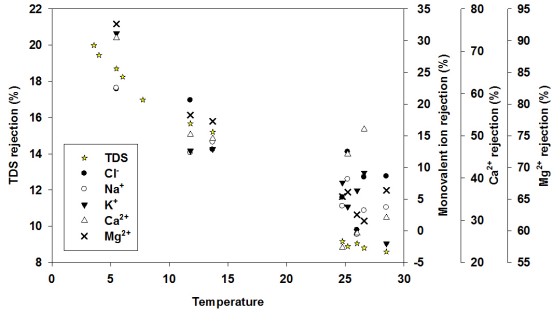


Fig. 5. Effect of temperature on the TDS, monovalent and divalent ions rejection (%) in NF system. % SO42− rejection was not shown in this figure, but, sulfate rejection was from 96 % at 28.5 ° C to 99 % at 5 ° C.

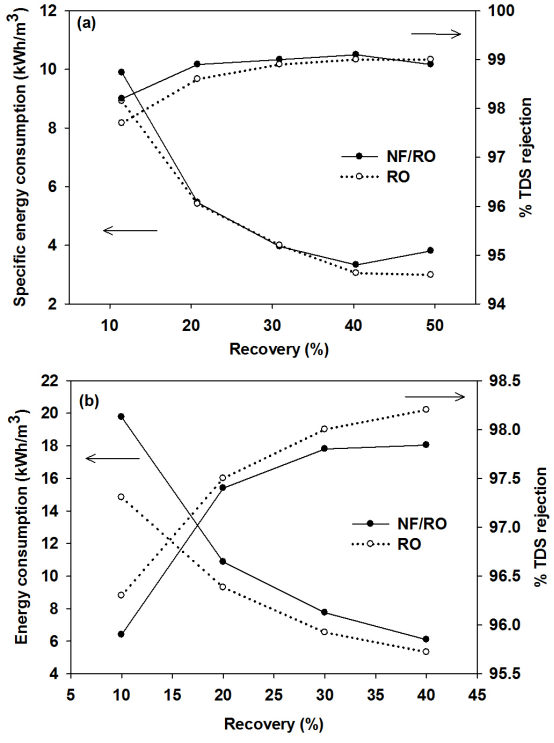


Fig. 6. Energy consumption and salt rejection of NF/RO hybrid system and only RO system for (a) seawater only and (b) designed seawater with different recoveries (NF recovery was set to 80 % and RO recovery was 10~40 %, Qf = 40 m3/d, All data are compensated at 25 ℃).

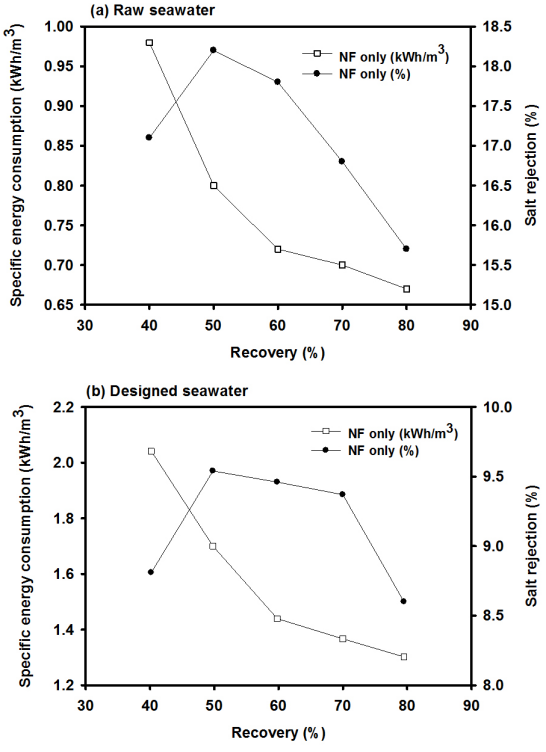


Fig. 7. Specific energy consumption and salt rejection (%) of NF only system for (a) raw seawater and (b) designed seawater samples with various recovery ratio.

4_CONCLUSIONS

Combined system of NF/RO membranes, was demonstrated for desalination, as compared to only-RO system, to identify some advantages in ion rejection performance (especially divalent ions) and system efficiencies. Even though no further scaling formation test or investigation into the foulant type were carried out, the system revealed increased water qualities of treated feedwaters, in terms of divalent ions (including sulfate, magnesium, and calcium) especially at higher system recoveries at 80 % for NF and 40 % for RO. Effects of increased permeate flux with varying system recovery, and of water temperature on energy efficiency and ion rejection were demonstrated: either diffusion- or convection-dominant transport was identified using the ion rejections patterns of RO and NF membranes, respectively. The approaches adopted in this study can be further used to optimize both efficiency and effectiveness of the combined NF/RO system for better desalination, under varying operating conditions, even with different membranes.

REFERENCES

1. K.P. Lee, T.C. Arnot and D. Mattia, A review of reverse osmosis membrane materials for desalination—Development to date and future potential, J. Membr. Sci., 370 (2011) 1–22.
2. C. Fritzmann, J. Löwenberg, T. Wintgens and T. Melin, State-of-the-art of reverse osmosis desalination, Desalination, 216 (2007) 1–76.
3. 24th IDA Worldwide Desalting Plant Inventory, 2012.
4. A.P. Mairal, A.R. Greenberg and W.B. Krantz, L.J. Bond, Real-time measurement of inorganic fouling of RO desalination membranes using ultrasonic time-domain reflectometry, J. Membr. Sci., 159 (1999) 185–196.
5. M. Busch and W. Mickols, Reducing energy consumption in seawater desalination, Desalination, 165 (2004) 299–312.
6. C.A.C. van de Lisdonk, J.A.M. van Paassen and J.C. Schippers, Monitoring scaling in nanofiltration and reverse osmosis membrane systems, Desalination, 132 (2000) 101–108.
7. L. Llenas, G. Ribera, X. Martínez-Lladó, M. Rovira and J. de Pablo, Selection of nanofiltration membranes as pretreatment for scaling prevention in SWRO using real seawater, Desalin. Water. Treat., 51 (2012) 930–935.
8. F. Dutoy and W. van der Wal, Successful antiscalant field trial — Optimization at higher pH and seawater temperature — Larnaca Desalination Plant, Desalin. Water. Treat., 31 (2011) 311–319.
9. P. Eriksson, M. Kyburz and W. Pergande, NF membrane characteristics and evaluation for sea water processing applications, Desalination, 184 (2005) 281–294.
10. A.A. Al-Hajouri, A.S. Al-Amoudi and A.M. Farooque, Long term experience in the operation of nanofiltration pretreatment unit for seawater desalination at SWCC SWRO plant, Desalin. Water. Treat., 51 (2012) 1861–1873.
11. L. Llenas, X. Martínez-Lladó, A. Yaroshchuk, M. Rovira and J. de Pablo, Nanofiltration as pretreatment for scale prevention in seawater reverse osmosis desalination, Desalin. Water. Treat., 36 (2011) 310–318.
12. G.F. Leitner, Breaking the cost barrier for seawater desalting, Int. Desalin. Water Reuse Q., 8 (1998) 15–20.
13. S. Avlonitis, Operational water cost and productivity improvements for small-size RO desalination plants, Desalination, 142 (2002) 295–304.
14. M. Darwish, F. Al Asfour and N. Al-Najem, Energy consumption in equivalent work by different desalting methods: case study for Kuwait, Desalination, 152 (2003) 83–92.
15. E. Drioli, A. Criscuoli and E. Curcio, Integrated membrane operations for seawater desalination, Desalination, 147 (2002) 77–81.
16. E. Drioli, E. Curcio, G. Di Profio, F. Macedonio and A. Criscuoli, Integrating membrane contactors technology and pressure-driven membrane operations for seawater desalination: energy, exergy and costs analysis, Cheml. Eng. Res. Des., 84 (2006) 209–220.
17. M. Nilsson, G. Trägårdh and K. Östergren, The influence of pH, salt and temperature on nanofiltration performance,

J. Membr. Sci., 312 (2008) 97–106.

18. F.G. Donnan, Theory of membrane equilibria and membrane potentials in the presence of non-dialysing electrolytes. A contribution to physical-chemical physiology, J. Membr. Sci., 100 (1995) 45–55.
19. N. Park, B. Kwon, M. Sun, H. Ahn, C. Kim, C. Kwoak, D. Lee, S. Chae, H. Hyung and J. Cho, Application of various membranes to remove NOM typically occurring in Korea with respect to DBP, AOC and transport parameters, Desalination, 178 (2005) 161–169.
20. R.R. Sharma, R. Agrawal and S. Chellam, Temperature effects on sieving characteristics of thin-film composite nanofiltration membranes: pore size distributions and transport parameters, J. Membr. Sci., 223 (2003) 69–87.
21. K. Plakas, A. Karabelas, T. Wintgens, and T. Melin, A study of selected herbicides retention by nanofiltration membranes—the role of organic fouling, J. Membr. Sci., 284 (2006) 291-300.
22. K.L. Tu, L.D. Nghiem, and A.R. Chivas, Coupling effects of feed solution pH and ionic strength on the rejection of boron by NF/RO membranes, Chem. Eng. J., 168 (2011) 700-706.
23. C.Y. Tang, Y.N. Kwon, and J.O. Leckie, Fouling of reverse osmosis and nanofiltration membranes by humic acid—effects of solution composition and hydrodynamic conditions, J. Membr. Sci., 290 (2007) 86-94.
24. A. Widjaya, T. Hoang, G.W. Stevens, S.E. Kentish, A comparison of commercial reverse osmosis membrane characteristics and performance under alginate fouling conditions, Sep. Purif. Technol., 89 (2012) 270-281

발전 배출가스 직접반응을 통한 CO_2포집 및 대량활용 저장기술 개발

Development of process technology for CO_2 capture and utilization through direct reaction of gas emitted from power plants

김병환
플랜트환경연구팀 수석연구원
byunghwan.kim@daewooenc.com

김정헌
플랜트환경연구팀 선임연구원
jeongheon.kim@daewooenc.com

강필선
플랜트환경연구팀 전임연구원
pilsun.kang@daewooenc.com

유승관
플랜트환경연구팀 전임연구원
seungkwan.yoo@daewooenc.com

Abstract

Mineral carbonation is one of the safest permanent CO_2 sequestration methods. CCU(Carbon Capture & Utilization) is a process to use available resources by removing carbon dioxide in a method of mineral carbonation. It can be applied to the industry for carbon dioxide emissions.

In this study, CO_2 fixation was carried out on the Daewoo Elimination of CO_2(DECO2) system (3,500Nm^3/h pilot plant scale reactor). Calcium hydroxide suspension was used as an absorbent. Ambient temperature and pressure were maintained during the whole process. As a result of absorption experiments, CO_2 removal efficiency of absorbent added NaOH increased from 30% to 90% with an increase of additive from 1 wt% to 3wt%. Also, CO_2 removal efficiency of continuous operation test was about 90%.

Keywords : Mineral carbonation, CCS, CO_2 fixation, $Ca(OH)_2$

1_서론

국가온실가스 배출목표가 2014년 6.6억톤에서 2020년 5.4억톤으로 설정되어 있고[1], 2020년까지 BAU대비 30% 국가 온실가스 감축 목표시한이 도래하고 있으나, 국내 여건에 맞는 CCS 기술개발이 완성되지 못하고 있는 실정이다. 기존의 탄산화 연구는 반응을 이용한 CO_2 포집에 주안점을 두고 있으나, 반응 전환물을 저장하는데 한계가 있어 온실가스 감축실적과의 연계가 어려웠다. CO_2를 줄이기 위해서는 에너지 효율향상, 신재생에너지 활용, 원자력 등 비 화석연료를 활용한 에너지 생산 방법이 사용되어 질 수 있으나, 화석연료 연소 배출가스에서 발생하는 CO_2를 직접 포집하여 육상 또는 해상의 하부에 저장하는 CCS (Carbon dioxide Capture and Storage) 기술사용이 불가피한 상황이다[2]. 그러나 우리나라의 경우 CO_2 포집기술은 활발히 개발되고 있으나, 포집된 CO_2를 육상 또는 해상에 저장할 수 있는 공간을 찾기가 쉽지 않고, 해외 이송 등 저장에 많은 비용이 소요될 전망이다. 따라서 CO_2를 직접 포집함과 동시에 최종 저장까지 완결할 수 있을 뿐 아니라 CO_2 저장 잠재량이 일정규모 이상의 대량포집 및 건설소재 활용 기술개발이 필요하다[3]. 이를 해결하기 위하여 기존의 CCS공정을 대체할 수 있는 CO_2 포집 원료화 공정을 개발 하였다. DECO2(Daewoo Elimination of CO_2)공정은 발전소 등 배출가스의 CO_2를 포집하고, 이때 발생하는 부산물을 토목 및 건축 소재로 활용할 수 있는 기술로 현장적용성이 뛰어나고, 경제성이 우수한 효율적인 공정이라 할 수 있다. 본고에서는 개발된 DECO2 공정의 현장 적용성과 Scale up에 필요한 핵심 변수별 운영특성을 파악하기 위하여, 일일 CO_2 10톤급 파일럿 플랜트의 현장적용을 통한 연속운전데이터와 흡수제별 CO_2 포집성능을 확인하고자 하였다.

2_CO_2 포집 원료화 공정개요

DECO2공정의 원리는 Fig. 1에서와 같이, 발전소 등 배출가스 속에 들어있는 CO_2 (10~15%)를 고속탄산화 반응기에서 연속 포집하여 배출가스 속의 CO_2를 제거하게 된다. 이때 반응약제로 사용하는 Ca와 같은 광물물질은 DECO2 탄산화반응기에서 CO_2와 반응하여 탄산칼슘($CaCO_3$)을 생산하고, 탄산칼슘은 시멘트대체재, 지반개량제, 탈황제 등으로 활용될 수 있다. 이 공정은 일반적으로 광물탄산화 공정(Mineral carbonation)으로 알려져 있으며, CO_2를 영구적으로 저장할 수 있기 때문에 육상이나 해상에 직접 저장하는 것보다 더 안전하게 저장할 수 있는 방법이라고 할 수 있다. 여기서 핵심 공정은 DECO2 고속 탄산화 반응기로 주요 장치의 기본 구성은 Fig. 2와 같다. 미세버블 반응기 내부에는 수산화칼슘($CaOH)_2$과 첨가제(NaOH 등) 현탁액으로 채워져 있으며, 유입가스 미세버블 분배기가 설치되어 있어, 고효율로 CO_2를 포집하며, pH 센서 및 레벨게이지를 이용하여 연속운전이 가능하다.

3_연구방법

처리대상 가스는 Fig. 3과 같이 인천광역시 서구 경서동 인천환경공단 청라사업소에 배출되는 가스로서, 전체 80,000Nm^3/h 중 4% 정도인 3,500Nm^3/h 만 본 공정에 도입되었다. 유입가스는 N_2, CO_2, O_2, H_2O, SOx, NOx, HCl 등으로 구성되어 있고, CO_2의 농도는 8~10%정도로 유동적이었다. 1,2차 반응기의 온도에 따라 CO_2포집 효율을 측정하였고, 이후, 반응기 수두별, 첨가제로 사용한 NaOH의 농

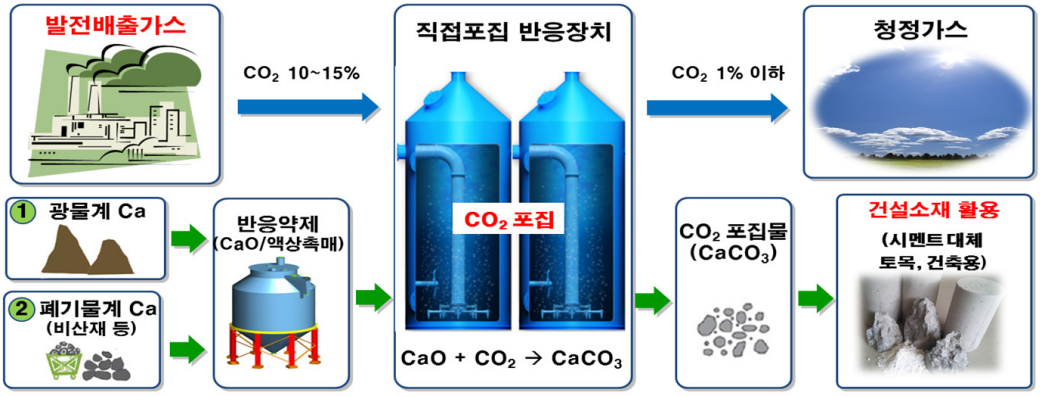


Fig. 1. CO_2 포집 원료화 공정 원리

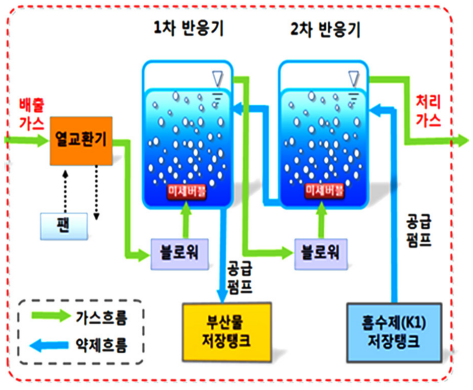


Fig. 2. DECO2 공정의 흐름도



Fig. 3. 10톤 CO_2/일 DECO2 Pilot Plant

도별 CO_2 포집 효율을 측정하였다. 연속운전의 특성을 파악하기 위하여 50시간 연속운전을 실시하였으며, 흡수제의 종류를 변화시키며 효율을 확인하였다.

4_결과 및 고찰

4.1 운영일자별 CO_2처리효율 및 처리량 변화

운영기간동안의 일별 처리 효율을 Fig. 4에 나타내었다. 일일 사용된 흡수제와 운전 시간에 따라 CO_2 처리량과 처리효율이 다르게 나타나고 있다. CO_2 제거 효율이 가장 낮을 때는 31.23%였으며, 이는 사용흡수제를 pH가 낮아져도 교환하지 않고 지속적으로 사용한 결과이다. 이와 반대로 CO_2 제거효율이 가장 높을 때는 97.73% 으로 나타나고 있다. CO_2 입구 농도는 약 8% 정도로 일정하였으며, 출구농도는 0.18 ~ 3.35%정도로 제거효율에 따라 다르게 측정 되었다. 사용된 흡수제와 운영조건에 따라 다르게 나타났으며, 전체운영기간 평균 80% 이상의 우수한 제거효율을 보이고 있다.

4.2 사용 흡수제별 제거효율 변화

본 실험은 흡수제 종류에 따른 CO_2제거 효율을 확인하기 위하여 실시하였다. 수두높이를 2m로 고정시켰고, 가스 유입유량은 약 3,500m^3/h이고, CO_2 유입농도는 약 8~10%로 측정되었다.

사용 흡수제별 CO_2 제거 효율을 Table 1에 나타내었다. K1-20B-G0.0에서 K1은 Ca(OH)2와 NaOH를 혼합한 흡수제명이며, 20에서 20은 $Ca(OH)_2$의 wt%를 나타내며 B는 500mesh particle size를 가지는 흡수제를 명하고, A는 1000mesh를 나타낸다. 각각의 G0.0~2.0은 첨가된 NaOH의 wt%를 의미한다.

Fig. 5에서는 흡수제별 CO_2 제거효율 및 제거량을 그래프로 나타내었다. 흡수제에 첨가된 NaOH의 양이 증가할수록 제거효율이 증가하는 것을 확인할 수 있었다. NaOH를 전혀 넣지 않았을 경우에는 약 60%의 제거효율을 보이며, 2wt%를 첨가하였을 경우 96%정도의 효율을 나타내는 것을 확인할 수 있었다. Particle size별로도 실험을 하였으며 particle size가 500, 1000mesh 두 경우 모두 약 96%

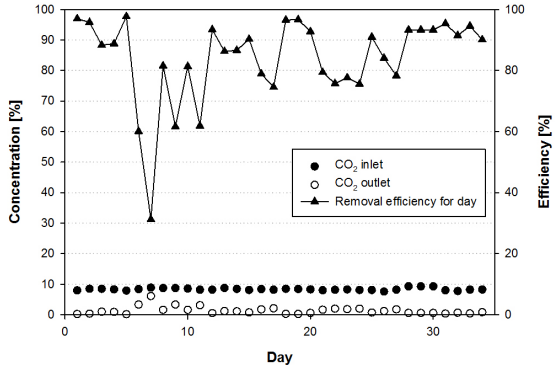


Fig. 4. 운영일자별 CO_2 포집효율 그래프

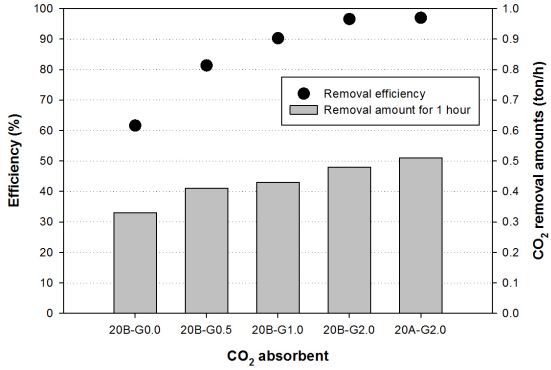


Fig. 5. 흡수제별 CO_2 제거효율 및 제거량

Table 1. 사용 흡수제에 따른 제거효율

No.	사용흡수제	CO_2 평균농도 (%)		처리효율 (%)	일일처리량 (CO_2 ton)	운전시간 (min)	시간당 CO_2처리량 (ton/h)
		유입가스	배출가스				
1	K1-20B-G0.0	8.73	3.35	61.63	1.36	250	0.33
2	K1-20B-G0.5	8.58	1.60	81.35	1.8	262	0.41
3	K1-20B-G1.0	8.12	0.79	90.27	2.69	375	0.43
4	K1-20B-G2.0	8.48	0.29	96.58	2.03	254	0.48
5	K1-20A-G2.0	7.96	0.24	96.98	1.03	122	0.51

의 제거효율을 보이며, particle size에 영향은 거의 없는 것으로 판단되어 진다. NaOH의 양이 증가할수록 효율 증가와 함께 시간당 CO_2처리량도 증가하는 것을 확인할 수 있었다. NaOH가 전혀 첨가되지 않았을 경우는 0.33ton/h를 나타내었으며, 첨가량이 2.0wt%까지 증가하였을 경우 0.48ton/h까지 증가하는 것을 확인할 수 있었다.

4.3 50시간 연속운전 제거효율 변화

본 실험은 인천환경공단 청라사업소에서 배출되는 가스 중 약 3,500Nm³/h의 유입가스를 50시간 연속적으로 DECO2 공정에 유입시켜 연속운전 처리효율을 확인하기 위한 실험이었다. Table 2에는 연속운전 운영 결과표를 보여주고 있다. 2013년 2월 26일 10시 20분부터 2월 28일 12시 20분까지 3일간 연속적으로 시설을 가동하였으며 전체 시설 가동시간은 50시간이었고 같은 기간 가스의 유입처리 총 누계량은 163,181Nm³로 평균 3,264Nm³/h의 가스를 유입처리 하였다. 사용된 흡수제는 K1(20wt%)를 사용하였고, 첨가제는 NaOH 1wt%를 사용하였다.

Table 2에서 확인할 수 있는 것과 같이 CO_2 처리 누계량은 총 27.87톤이며, 평균 0.56톤/h의 CO_2를 제거한 것으로 나타났으며, 본 시설을 24시간 연속운전으로 환산할 경우 13.38톤/일의 CO_2 제거가 가능한 것을 알 수 있다. 입 평균 유량은 3,264Nm³/h으로 측정되었으며, CO_2제거율은 50회 평균(시간당 1회 측정 X 50회) 93.3%인 것으로 나타났다.

연속운전기간 동안 사용된 흡수제는 총 205톤이 사용되었고, 27.87톤의 CO_2가 포집되었다. 이는 CO_2 1톤을 처리를 위해 흡수제 약 7.35ton이 필요한 것으로 분석되었다. 부산물은 총 197.5톤 정도 발생하였다.

Fig. 6에는 연속운전 CO_2 제거효율 그래프를 나타내었다. 유입되는 가스의 CO_2 농도는 8~10%로 측정되었으며 CO_2 인입 평균 농도는 9.30%로 측정되었고, DECO2 P/P에서 제거 후 배출되는 CO_2는 평균 0.62%로 측정되었다. 50시간 연속운전동안 평균 90% 이상의 제거효율로 CO_2가 처리되는 것을 확인하였다.

Table 2. 연속운전 결과표

구 분	가스유입량	운영시간	처리량
1시간 평균(/h)	3,264 Nm³	1시간	0.56 CO_2톤
1일 평균(/day)	78,327 Nm³	24시간	13.38 CO_2톤
50시간 총 계	163,181 Nm³	50시간	27.87 CO_2톤

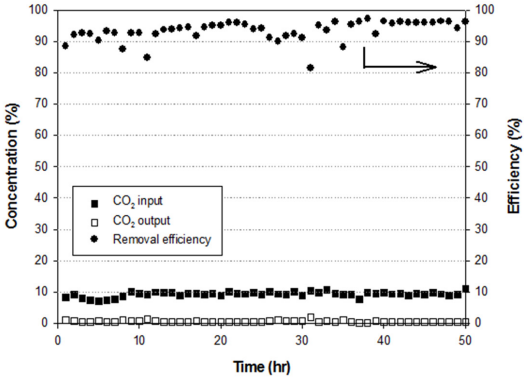


Fig. 6. 연속운전 CO_2 제거효율 그래프

5_결 론

1) 운영기간동안의 처리효율을 확인한 결과, CO_2 제거 효율이 가장 낮을 때는 31.23%였으며, 이는 사용흡수제를 pH가 낮아져도 교환하지 않고 지속적으로 사용한 결과이다. 또한 CO_2 제거효율이 가장 높을 때는 97.73% 으로 나타났다. 사용된 흡수제와 운영조건에 따라 다른 결과를 보였으며, 전체운영기간 평균 80% 이상의 우수한 제거효율을 보였다.

2) 흡수제에 첨가된 NaOH의 양이 증가할수록 제거효율이 증가하는 것을 확인할 수 있었다. NaOH를 전혀 넣지 않았을 경우에는 약 60%의 제거효율을 보이며, 2wt%정도 첨가하였을 경우 약 96%의 제거효율을 나타내는 것을 확인할 수 있었다. Particle size에 따른 결과 500, 1000 mesh 두 경우 모두 약 96%의 제거효율을 보이며, particle sized의 영향은 거의 없는 것으로 판단되어 진다. 또한 NaOH의 양이 증가할수록 효율 증가와 함께 시간당 CO_2처리량도 증가하는 것을 확인할 수 있었다.

3) 유입되는 가스의 CO_2 농도는 8~10%로 측정되었으며 CO_2 인입 평균 농도는 9.30%로 측정되었고, DECO2

P/P에서 제거 후 배출되는 CO_2는 평균 0.62%로 측정되었다. 50시간 연속운전동안 평균 90% 이상의 제거효율로 CO_2가 처리되는 것을 확인하였다.

참고문헌

1. 2014년 에너지기술 이노베이션 로드맵, 에너지기술평가원 (2014)
2. Carbon Dioxide Capture and Storage, IPCC Special Report (2005)
3. CO_2 활용 · 처리 건설재료 기술 기획보고서, 한국건설교통기술평가원 (2011)

Simplified method for estimating the effect of a hydrogen explosion on a nearby pipeline

방부형
플랜트환경연구팀 전임연구원
boohyoung.bang@daewooenc.com

본 논문은 2016년 Journal of Loss Prevention in the Process Industries Vol.40, pp. 112–116에 게재되었던 논문을 재게재한 것입니다.

Abstract

To predict the effect of hydrogen gas tank explosions on nearby pipelines, we first evaluate the increase in air pressure and velocity on a pipeline after a strong explosion. Then, we calculate the bending of an initially straight pipe. We investigate the bending amplitude for various exploded masses of hydrogen, distances measured from the explosion center to the pipeline, and thicknesses of steel pipeline walls. The proposed analytic approach provides a conservative estimate of the worst-case accident scenario involving an instantaneous explosion of a large hydrogen mass leading to the formation of a shock wave. The results may be useful for plant engineers to evaluate the risks associated with pipelines under the presumed explosion scenario of not only hydrogen, but also any other fuel types.

Keywords : Explosion, Overpressure, Shock wave, Pipeline

1_INTRODUCTION

Any off- or on-shore plant of petrochemical and refinery type incorporates pipelines located in the vicinity of tanks containing flammable liquids or gases. Though these structures are regularly monitored and undergo safety maintenance, potential leakage of flammable substances is always possible because the plant structures are typically subjected to corrosive environment which causes structural damages and potential malfunction in equipment over time. A potential leakage can result in explosion which would jeopardize lives and inflict large economic losses. Therefore, an estimate of potential damage caused by such explosions is important.(Jo & Ahn, 2002 Sklavounos & Rigas, 2006 J. R. Taylor, 2003)In the case of explosions accompanying leakage of explosive substances from tanks located close to pipelines, the question to be addressed is whether these pipelines can survive an impact of shock wave generated by such explosions.

The classical self-similar theory of the strong explosion can estimate the pressure, gas velocity, and density at the shock wave front for a given large mass of fuel which exploded (von Neumann, 1963 Sedov, 1946, 1993 Taylor, 1950a, 1950b) see also the general fluid mechanical texts (Landau & Lifshitz 1987; Yarin 2007). These information can be used to evaluate loads applied on the surrounding pipelines and, in particular, predict their bending expected at the distances corresponding to their location from the explosion center (Rigas & Sebos, 1998). The outcome of such evaluations should affect design of petrochemical and refinery plants to avoid the worst-case scenarios.

In addition, to the analytic tools, pressure rise resulting from explosions of different massed of fuel can also be predicted by com-

putational codes, e.g. such as EXSIM(Explosion SIMulator) and FLACS (Flame ACceleration Simulation) (Lea & Ledin, 2002). However, FLACS is limited only to deflagration cases and cannot be extended to model detonation or fast deflagration scenarios. For this reason, here we discuss an analytical method which predicts the pressure rise as a result of strong instantaneous explosion and shock wave formation and propagation for an unconfined environment. The theory is inapplicable to highly-congested environments.

2_THE STRONG EXPLOSION THEORY

The proposed analytic approach describes in this section considers the worst-case accident scenario of an instantaneous explosion of a large hydrogen mass leading to formation and propagation of a strong shock wave. The classical theory of strong explosions specifies, among other parameters, the pressure, P_{sh}, gas velocity, V_{sh}, and density, ρ_{sh}, at the shock wave front as in Refs. (Landau & Lifshitz, 1987 von Neumann, 1963 Sedov, 1946 Sedov, 1993 Taylor, 1950a, 1950b Yarin, 2007):

$$P_{sh} = \frac{8\rho_a}{25(\gamma+1)}\left(\frac{E_0}{\rho_a}\right)^{2/5}\frac{1}{t^{6/5}}, \quad (1)$$

$$V_{sh} = \frac{4}{5(\gamma+1)}\left(\frac{E_0}{\rho_a}\right)^{1/5}\frac{1}{t^{3/5}}, \quad (2)$$

and

$$\rho_{sh} = \frac{(\gamma+1)}{(\gamma-1)}\rho_a. \quad (3)$$

where E_o denotes the total energy released in the explosion, ρ_a is the air density before the shock wave, γ is the ratio of the specific heat at constant pressure to the specific heat at constant volume (of air), and t is time from the moment of explosion, which is considered to happen instantaneously and pointwise at $t = 0$. This theory implies an instantaneous pointwise explosion of such strength that the pressure created behind the shock wave propagating from the explosion center is so high, that the atmospheric pressure before the shock wave can be neglected. This theory was independently developed by J. von Neumann (von Neumann, 1963), L.I. Sedov (L. I. Sedov, 1946 1993) and G.I. Taylor (Taylor, 1950a, 1950b) (the work of von Neumann was published long after his original result), and is discussed in brief in general books on fluid and gas dynamics (Landau&Lifshitz, 1987 Yarin, 2007).

Accordingly, the front of the shock wave, which is spherical when unaffected by obstacles, r_{th}, is

$$r_{sh} = \frac{2}{(\gamma+1)}\left(\frac{E_0}{\rho_a}\right)^{1/5} t^{2/5}. \quad (4)$$

The strong-explosion theory is based on the assumption that the explosion energy, E_0, is released instantaneously at a point, and is much higher than the atmospheric pressure. This implies that fuel is instantaneously evaporated and mixed with the oxidizer, and the reacting mixture is stoichiometric. The theory also neglects energy losses due to thermal radiation- the entire released energy is converted into the energy of shock wave and the accompanying gas motion. These assumptions tend to overestimate the strength of the shock wave. In reality, liquid hydrogen spillage and evaporation, for example, will take some time and space, and are accompanied by liquid atomization (losses). Also, mixing with the oxidizer (oxygen in air) can be far from complete when the explosion occurs, and nitrogen in air will act as a thermal ballast. Typically, a fuel-oxidizer mixture will be lean (not pre-mixed). These factors diminish the strength of a real shock wave compared to the idealized predictions of the theory of strong explosion. The strong-explosion theory is purely gasdynamical and does not consider turbulent eddy viscosity and the effect of turbulence on the energy-release rate or gas motion. With all the simplifying assumptions listed above, the first estimates of the strong explosion effects should be based on the strong-explosion theory outlined above.

Based on Eq. (4), the time required for the shock wave to reach a pipe located a distance L from the center of explosion is:

$$t = L^{5/2}\left(\frac{\gamma+1}{2}\right)^{5/2}\frac{1}{(E_0/\rho_a)^{1/2}}. \quad (5)$$

Then, according to Eqs. (1), (2) and (5), pressure and velocity at the shock-wave front as it contacts the pipe are

$$P_{sh,L} = \frac{64}{25}\frac{1}{(\gamma+1)^4}\frac{E_0}{L^3}, \quad (6)$$

and

$$V_{sh,L}=\frac{4\sqrt{8}}{5}\frac{1}{(\gamma+1)^{5/2}}\frac{1}{L^{3/2}}\left(\frac{E_0}{\rho_a}\right)^{1/2} \tag{7}$$

Denoting the pipe diameter as 2a, with a being the cross-sectional radius, and using Eq. (2), we find the time ΔT required for the shock wave front to cross the pipe as

$$\Delta T=5a\left(\frac{\gamma+1}{2}\right)^{5/2}\frac{L^{3/2}}{(E_0/\rho_a)^{1/2}} \tag{8}$$

3_CALCULATION OF PIPE BENDING

Equations of the pipeline dynamics are well-known (Svetlitskii, 1982 V.M. Entov, 1987), and in the simplest case of planar bending of an initially straight pipe, they can be reduced in the first approximation to the following bar-bending-like equation

$$(\rho_1 f_1+\rho_2 f_2)\frac{\partial^2 H}{\partial t^2}+EI_1\frac{\partial^4 H}{\partial x^4}=2a\Delta p_{dyn} \tag{9}$$

Here the pipe is assumed to be circular in cross-section; ρ_1 and ρ_2 are densities of the pipe wall and a gas or a liquid which can be inside; f_1 and f_2 are the cross-sectional areas occupied by the pipe material and the gas (or liquid) inside, respectively; H is the bending displacement, t is time (obviously different from t of section 2), E is Young's modulus of the pipe wall; I_1 is the moment of inertia of the pipe wall cross-section; x is the Cartesian coordinate reckoned along the axis of the unperturbed pipe; Δp_{dyn} is the dynamic pressure difference across the pipe.

The geometric parameters involved in Eq. (9) are found as

$$f_1=2\pi ah,\quad f_2=\pi a^2,\quad I_1=\pi a^3 h \tag{10}$$

where a is the pipe radius (not including the wall), and h is the wall thickness.

We search the solution of Eq. (9) in the following form

$$H=A(t)\sin kx \tag{11}$$

where $A(t)$ is the bending amplitude and k is the wavenumber ($k=2\pi/\lambda$, with $l=\lambda/2$ being the pipe length between two fixed sections).

Then, Eq. (9) yields

$$\left(\frac{d^2A}{dt^2}+\omega^2 A\right)\sin kx=\frac{2a\Delta p_{dyn}}{(\rho_1 f_1+\rho_2 f_2)} \tag{12}$$

where

$$\omega^2=\frac{EI_1(2\pi/\lambda)^4}{\rho_1 f_1+\rho_2 f_2} \tag{13}$$

The dynamic pressure drop acting on the pipe is associated with the shock wave front, as found in Eq. (6). It fades in time, as the shock wave passes the pipe cross-section, and has its maximum in the middle of the pipe length. Therefore, it is possible, in the first approximation to take

$$\Delta p_{dyn}=\left(p_{sh,L}+\frac{\rho_{sh}V_{sh,L}^2}{2}\right)\cos\omega t\sin kx \tag{14}$$

which is considered during the time period when $0\le\omega t\le\pi/2$.

Then, Eq. (12) is reduced to

$$\frac{d^2A}{dt^2}+\omega^2 A=F\cos\omega t \tag{15}$$

with F being given by the following expression

$$F=\frac{2a\left(P_{sh,L}+\rho_{sh}V_{sh,L}^2/2\right)}{\rho_1 f_1+\rho_2 f_2} \tag{16}$$

The solution of Eq. (15) subjected by the initial conditions

$$t=0:A=\frac{dA}{dt}=0 \tag{17}$$

yields the following result for the bending amplitude

$$A=\frac{F}{2\omega}t\sin\omega t \tag{18}$$

At short times, when $\omega t\ll 1$, the asymptotical behavior following from Eq. (18) is

$$A=\frac{F}{2}t^2 \tag{19}$$

The critical bending amplitude (or displacement) is normally determined by the design engineers who would consider different safety factors affecting the design. The engineers can utilize the model/theory provided herein to yield the most conservative estimate which would prevent the collapse of their pipe system in case of explosion.

4_CALCULATION OF PIPE SQUEEZING

According to (Timoshenko, 1961), a pipeline will be squeezed by the outside pressure $P_{sh,L}$ if

$$P_{sh,L} > P_{crit} = \frac{Eh^3}{4a^3(1-\nu^2)} \quad (20)$$

where ν is Poisson's ratio of pipe wall.

The inequality Eq. (20) implies an empty pipeline, or the one with pressure inside being relatively low compared to $P_{sh,L}$. It should be emphasized that a high internal pressure would just diminish the effect of $P_{sh,L}$, and the inequality Eq. (20) would be re-written for the pressure difference.

5_RESULTS AND DISCUSSION

Heat release in hydrogen explosion is associated with the reaction of hydrogen oxidation in air. The hydrogen specific heat release is Q = 120 MJ/kg at the LHV (Lower Heating Value) (Baker, Cox, Kulesz, Strehlow, & Westine, 2012). Then, the total energy released in hydrogen explosion is $E_0 = Q \cdot m$, where m is the hydrogen mass which has exploded. The other parameters of interest have the following values: the adiabatic index $\gamma = 1.4$, the air density $\rho_a = 1.21 \times 10^{-3}$ g/cm^3, the density of the pipe material $\rho_1 = 7.8$ g/cm^3 (steel), its Young's modulus E = 200 GPa (steel) and Poisson's ratio $\nu = 0.303$ (steel). We assume that the pipeline is empty, and thus take $\rho_2 = 0$.

First, the effect of hydrogen mass (m) on the bending amplitude (A) was studied, for which the distance between the point source and the pipe was L = 10 m; the pipe wall thickness was h = 1 cm; the pipe length was l = 10 m; and pipe cross-sectional radius was a = 0.24 m. Second, the effect of L on A was also studied under the fixed values of m = 1000 kg, h = 1 cm, l = 10 m, and a = 0.24 m. Last, the effect of wall thickness (h) was studied while using L = 10 m, m = 1000 kg, l = 10 m, and a = 0.24 m. Note, that it is assumed that while traveling the distance L, the shock wave have not impinges on any other obstacles, and the first such encounter is with the pipe under consideration. In a highly-congested environment this assumption might be inapplicable and the shock-wave could lose its strength on the wave to a pipe.

Notably, it should be emphasized that the pipe length was taken as a half of the wavelength ($l = \lambda/2$). Because the wavenumber is $k = 2\pi/\lambda$, the effect of the pipe length is incorporated in the argument of sine in Eq. (11). However, the sine function is at the end cancelled and does not appear in the F expression in Eq. (16) and thus l will not affect the bending amplitude, A. The bending amplitude is finally expressed in terms of F, as in Eq. (19), which is a function of the shock pressure ($P_{sh,L}$) and velocity ($V_{sh,L}$) from Eq. (16). One may also see that F depends on pipe geometry, namely, on a and h.

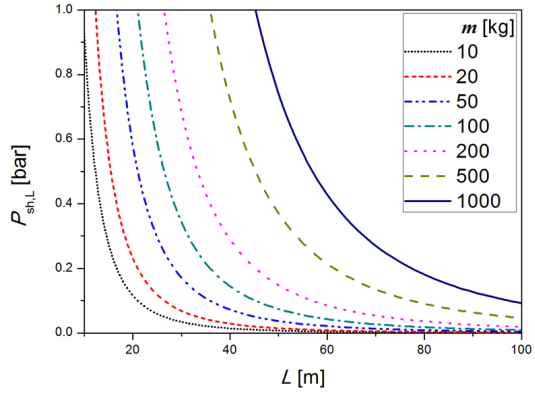


Figure 1 Pressure at the shock wave front versus distance to the explosion center for different exploded masses (m). The pipe wall thickness and radius were fixed at h = 1 cm and a = 0.24 m.

Figure 1 shows how the shock wave pressure depends on the distance (L) between the explosion center and the pipe location. When the shock wave propagates away from the explosion center (and L is increasing), pressure at the shock wave front reduces dramatically. Larger exploded mass of hydrogen, result in much larger pressures at the shock wave front as is seen in Figure 1. For example, if a pipeline is located beyond the distance of L = 60 m from the explosion center, the shock wave weakens and the pressure at its front is below $P_{sh,L} \sim 0.1$ bar for exploded masses less than m = 200 kg.

Figure 2 shows how the bending amplitude increases in time when a pipeline is affected by the compressed gas in the wake of the shock wave resulting from explosions of different masses of hydrogen at a distance of L = 10 m from the pipeline.

Table 1 illustrates how the shock wave enhances as the exploded mass of hydrogen increases. In Case 7 in the table, the shock wave pressure increased up to 92.6 bar when the mass of hydro-

Table 2. Cyclic loading test conditions

Case	Exploded mass, m [kg]	Shock wave pressure, $P_{sh,L}$ [bar]	Shock time, ΔT [s]	Squeezing condition, $P_{sh,L}/P_{crit}$
1	10	0.93	19.0110^{-4}	0.023
2	20	1.85	13.4410^{-4}	0.047
3	50	4.63	8.5010^{-4}	0.116
4	100	9.26	6.0110^{-4}	0.233
5	200	18.52	4.2510^{-4}	0.465
6	500	46.30	2.6910^{-4}	1.163
7	1000	92.60	1.9010^{-4}	2.325

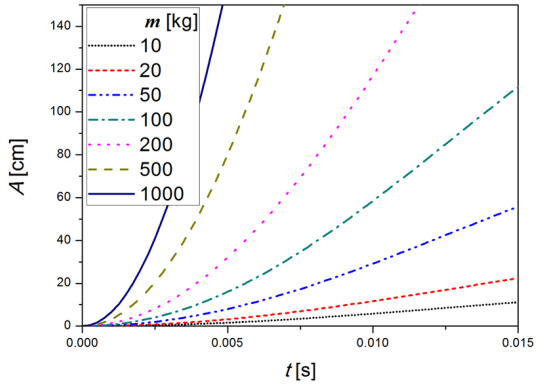


Figure 2. Bending amplitude versus time after the shock wave arrival for different exploded masses (m). The pipe wall thickness, cross-sectional radius, and distance from the explosion center are h = 1 cm, a = 0.24 m, and L = 10 m, respectively.

gen of 1000 kg exploded at the distance of L= 10 m. Then, the ratio of the squeezing gas pressure to the critical pressure for a pipeline with h = 1 cm, a = 0.24 m, L = 10 m, and l = 10 m is $P_{sh,L}/P_{crit}$ = 2.325. This ratio is well over unity, and thus an absolute destruction of the steel pipelines is guaranteed within 0.19 ms. In Case 5 in Table 1, the ration $P_{sh,L}/P_{crit}$< 1, which means that the steel pipelines would not fail. However, the shock wave pressure would increase up to 18.52 bar, which is high enough to destroy any concrete structure.

Figure 3 shows how the bending amplitude increases in time at various pipeline locations (L) after explosion of m = 1000 kg. As evident, the pipelines would definitely be bent and squeezed when they are close the explosion center. On the other hand, in cases of L > 100 m, the pipelines would not undergo severe bending. In petrochemical plants, the range of L of structures from potential

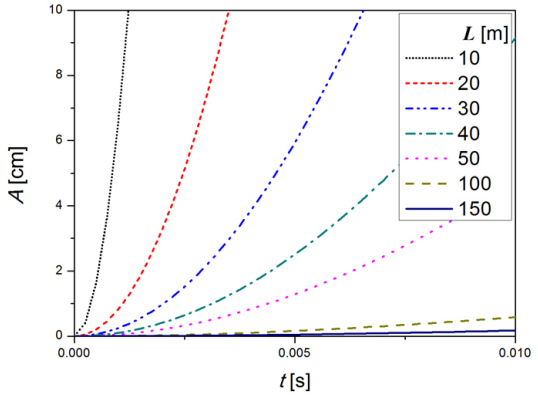


Figure 3. Bending amplitude versus time after arrival of the shock wave for different distances (L) to the explosion center when m = 1000 kg. The pipe wall thickness and radius were h = 1 cm and a = 0.24 m, respectively.

explosion centers is within a few to tens of meters. Thus, according to Figure 3, pipelines in such plants will be endangered, i.e. severely bent and squeezed, in the case of explosion of m = 1000 kg. The present analysis allows an estimate of a safe interspace distance between structures when designing a petrochemical plant.

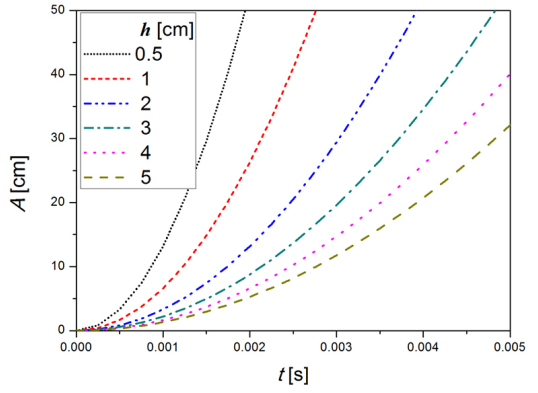


Figure 4. Bending amplitude versus time after arrival of the shock wave for different pipe wall thicknesses (h). The distance to the explosion center and cross-sectional radius of the pipeline were L = 10 m and a = 0.24 m, respectively. The hydrogen mass was m = 1000 kg.

Figure 4 illustrates the effect of the wall thickness of a pipeline on its bending amplitude following an explosion of m = 1000 kg at a distance of L=10 m. It is seen that bending of about 40 cm is possible even for pipes with the wall thickness of 5 cm under such conditions.

6_CONCLUSION

The most conservative estimate for pipe bending is established by employing the strong explosion theory. This conservative estimate is important for petrochemical plant engineers who need to provide the design parameters for their pipe location and characteristics for cases of unexpected explosion. These analytical equations are simple to use, unlike fully 3D direct numerical simulations, and therefore quick parametric studies can be conducted to yield design parameters with intended safety factors.

The explosion of m = 1000 kg of hydrogen resulting from a leakage from a tank, will be absolutely catastrophic for a pipeline located at a distance of L = 10 m from the explosion center: it will be bent and squeezed, and most probably completely destroyed. The pipeline will be also significantly bent due to the explosion of m = 100 kg of hydrogen. These results probably overestimate the explosion strength, since the explosion was considered to be instantaneous and pointwise, and all the factors leading to losses (atomization, radiation, turbulence, etc.) were neglected. Still, they provide a pretty realistic pattern of the effect of hydrogen explosion on a pipeline located L = 10 m apart. An increase in the distance between the hydrogen tank and the pipeline will diminish dramatically the effect of the explosion, since, the latter decreases as L^{-3}, i.e. doubling the distance diminishes the explosion effect 8 times.

ACKNOWLEDGEMENT

This research was primarily supported by Daewoo Institute of Construction and Technology. The research was also supported by NRF-2013R1A2A2A05005589, and International Collaboration Program funded by the Agency for Defense Development, and a special Korea University Grant. The author (S.S. Yoon) extends his appreciation to the Deanship of Scientific Research at King Saud University for its funding this Prolific Research Group (PRG-1436-03).

REFERENCES

1. Baker, W.E., Cox, P.A., Kulesz, J.J., Strehlow, R.A., & Westine, P.S. (2012). Explosion Hazards and Evaluation: Elsevier Science.
2. Jo, Y.-D., & Jong, A.B.. (2002). Analysis of hazard areas associated with high-pressure natural-gas pipelines. Journal of Loss Prevention in the Process Industries, 15(3), 179-188.
3. Landau, L.D., Lifshitz, E.M. (1987). Fluid Mechanics: volume 6 (Course of Theoretical Physics) Publisher: Bu: Butterworth-Heinemann.
4. Lea, C.J., & Ledin, H.S. (2002). A review of the state-of-the-art in gas explosion modelling: Health and Safety Laboratory.
5. von Neumann, J. (1963). The point source solution (Collected Works, vol. VI): Pergamon Press.
6. Rigas, F., & Sebos, I.. (1998). Shortcut estimation of safety distances of pipelines from explosives. Journal of transportation engineering, 124(2), 200-204.
7. Sedov, L. I. (1946). Propagation of strong blast waves. Journal of Applied Mathematics and Mechanics, 10, 241 - 250.
8. Sedov, L. I. (1993). Similarity and Dimensional Methods in Mechanics: CRC press.
9. Sklavounos, S., & Rigas, F. (2006). Estimation of safety distances in the vicinity of fuel gas pipelines. Journal of Loss Prevention in the Process Industries, 19(1), 24-31.
10. Svetlitskii, VA. (1982). Mechanics of pipelines and hoses. Mashinostroenie, Moscow.
11. Taylor, G. (1950a). The formation of a blast wave by a very intense explosion. I. Theoretical discussion. Proceedings of the Royal Society of London. Series A, Mathematical and Physical Sciences, 159-174.
12. Taylor, G. (1950b). The formation of a blast wave by a very intense explosion. II. The atomic explosion of 1945. Proceedings of the Royal Society of London. Series A, Mathematical and Physical Sciences, 175-186.
13. Taylor, J. R. (2003). Risk analysis for process plant, pipelines and transport: Routledge.

14. Timoshenko, S. (1961). Theory of elastic stability: Mc Graw-Hill.
15. Entov, V.M., Ty, F.K., & Yarin, A.L. (1987). On the equations of the off-shore pipeline.
16. Yarin, A.L. (2007). Self-similarity, Chapter 2.3 in Springer Handbook of Experimental Fluid Mechanics: Springer.